Journal of Porous Materials (2025) 32:1717–1728
https://doi.org/10.1007/s10934-025-01801-1

Large mesopore FDU- 12 silica for papain encapsulation

L. C. Cides-da-Silva[1] · D. W. Losito[2] · D. R. O. Pimentel[2] · N. Andreo-Filho[2] · T. S. Martins[2] · L. Otubo[3] · O. A. Sant´Anna[4] · M. C. A. Fantini[1]

Published online: 15 April 2025

Abstract
The usual synthesis of face-centered cubic FDU- 12 mesoporous silica reported in the literature does not mention the role of some experimental conditions that govern its structural and textural properties. In particular, the order of introducing the silica source into the reaction medium, the closing of the recipient setup, the concentration of the swelling agent, as well as the more researched influence of heat treatment on the material characteristics. In this study, the results indicated that the homogenization of F127 and TMB is essential before the introduction of TEOS into the reaction chamber to obtain a more ordered porous structure. This, together with maintaining the nominal concentrations of all chemical compounds by properly isolating the reaction chamber from the outside atmosphere, was crucial. The evaluation of TMB concentration revealed that the increase of TMB resulted in increased surface area, pore volume, and size, leading to entrance pores of different sizes, related to different amounts of TMB inside the F127 micelles. The best structural/textural results were achieved by a hydrothermal treatment (HT) of 100 °C, while higher HT increased pores sizes, but it raised disorder. Finally, the papain incorporation in the silica matrix preserved its catalytic properties and induced better catalytic activity, with around 42% higher efficiency than the isolated enzyme. The evaluation of papain delivery showed rapid release within one hour, followed by a slow, continuous release over time, finishing in 1 h.

Keywords FDU-12 · Cubic mesoporous silica · Papain · Enzyme activity

1 Introduction

Since the discovery of ordered mesoporous silica (OMS) by the researchers of the Mobil Company in 1992 [1, 2], significant progress has been made in the synthesis, characterization, and applications of OMS. These materials can be prepared using either ionic or nonionic surfactant templates. Nonionic surfactants offer several advantages over ionic surfactants, including biodegradability, commercial availability, low cost, and low toxicity [3, 4].

Ordered mesoporous materials have many potential applications, including adsorption of molecules and compounds, heterogeneous catalysis, sensors, separation chemistry, drug delivery, nanoscience, biotechnologies, and more recently, in the field of immunology, with advances in the research of oral vaccines [5–8].

Various ordered porous networks can be formed, such as cage-like structures with smaller entrance sizes compared to their internal reservoir [9–15], making them interesting for time-controlled absorption and release of specific substances. The morphology of the cubic and hexagonal structures can affect the release characteristics, such as the amount of material and release rate in time. The hexagonal structure has straight channels (~ 10 nm) with an open entrance a little smaller (~ 8 nm), while the cubic structure has a large cavity (~ 20 nm) and small entrances (~ 5 nm) that can interfere in the release speed. Researchers are particularly interested in matrices with cubic porous order, known as FDU- 1 and FDU- 12, due to their structure with

✉ L. C. Cides-da-Silva
luiscides@gmail.com

[1] Instituto de Física, Universidade de São Paulo, Rua Do Matão 1371, São Paulo, SP 05508 - 090, Brazil

[2] Instituto de Ciências Ambientais, Químicas e Farmacêuticas, Universidade Federal de São Paulo, Rua São Nicolau 210, Diadema, SP 09913 - 030, Brazil

[3] Instituto de Pesquisas Energéticas E Nucleares. Av. Professor Lineu Prestes 2242, Butantã, Sao Paulo, SP 05508 - 000, Brazil

[4] Instituto Butantan, Av. Vital Brazil 1500, São Paulo, SP 05503 - 900, Brazil

large mesopores of the order of ~ 20 nm, interconnected with mesoporous entrances of ~ 5 nm, which, like the cavities, can also be adjusted, by modifying some variables in the synthesis procedure. This class of mesoporous materials forms a three-dimensional (3D) network, exhibiting diffusional behavior distinct from the widely studied cylindrical mesoporous materials. It is generally accepted that ordered mesoporous materials with 3D mesoporous structures offer significant advantages in mass diffusion and transport compared to those with cylindrical mesopores. The successful use of these materials depends on controlling and adjusting the pore sizes (both cavities and entrances), ensuring high-quality textural and structural properties, and utilizing appropriate equipment for their synthesis. This research aims to (i) highlight and explain how some experimental conditions affect the structural and textural properties of this class of material and (ii) analyze their applicability in papain adsorption and release.

An appropriate combination of bioactive compounds within OMS is essential to guarantee that those substances keep their biological properties, including catalytic action when enzymes are the loaded molecules. The benefits of enzymes encapsulation or immobilization within silica matrices are well-documented in the literature, particularly concerning enhanced stability and enzymatic activity. It is mentioned, for example, the improvement on catalytic performance, depending on pH condition, for the hydrolysis of p-nitrophenyl glucopyranoside [16]. The strategy to immobilize enzymes in mesoporous silicates is indicated for applications in biocatalysis, biosensors and biofuel cells [17]. Another example includes fuel bioethanol production using β-glucosidase, in which the composite with silica proved to be an efficient biocatalyst, decreasing enzyme waste [18].

In this context, papain, a proteolytic enzyme, belonging to the cysteine-proteases class, awakes great interest for industrial and therapeutic uses, the latter especially as debriding on skin wounds caused by burning or continuous pressure on the tissue, contributing to healing by removal of the dead tissue, and favoring the arising of new cells and tissue regeneration [19].

Many relevant papers reporting the FDU- 1 or FDU- 12 synthesis processes do not mention the moment at which the silica source is introduced into the prior solution, neither the influence of this moment on the size of the pore entrance [9–15]. Also, the swelling agent conditions, like type, concentration and addition time to the synthesis vessel have not been valued in the resulting material properties. Usually, the concern about the influence of time in the material characteristics is related to the hydrothermal treatment process. Huang and Kruk [20] addressed the influence of the time when the silica source and toluene swelling agent are added to the reaction system, considering long periods of 27 h. They found that very strict conditions contribute to producing large pore samples. In the present research a detailed shorter schedule insertion step of TMB and TEOS in the synthesis vessel was analyzed by controlling two conditions, keeping the mass ratio of TMB/F127 constant, equal to 1:1. These two conditions were (i) simultaneous addition of TMB and TEOS (SA) and (ii) addition of TEOS after two hours of TMB inclusion (A2).

2 Materials and methods

2.1 Chemicals

Tetraethylorthosilicate (TEOS, 98%, Sigma-Aldrich), poly(ethylene oxide)–poly(propylene oxide)–poly(ethylene oxide) (Pluronic F127®, $PEO_{100}PPO_{65}PEO_{100}$, Sigma-Aldrich), hydrochloric acid (HCl, 37%, Merk), Potassium Chloride (Sigma Aldrich), nitric acid, HNO_3, (Sigma Aldrich), silver nitrate, $AgNO_3$, (Synth, Brazil), 1,3,5 trimethylbenzene (TMB, 98%, Sigma Aldrich), Deionized water, Nα-Benzoyl-DL-arginine p-nitroanilide hydrochloride (Sigma-Aldrich®, St Louis, USA), Sodium phosphate dibasic heptahydrate P.A. (Synth, Diadema, Brazil), Disodium ethylenediaminetetraacetate dihydrate P.A. (Synth, Diadema, Brazil), L-cysteine hydrochloride P.A. (Synth, Diadema, Brazil) Papain from Carica papaya (30,000 USP-U/mg, EMD Chemicals Inc, San Diego, USA), Papain pharmaceutical grade (30,000 USP-U/mg stabilized with sodium disulfite, Emprove® Essential Merck, Darmstadt, Germany), Glacial acetic acid (Synth, Diadema, Brazil).

2.2 Synthesis of ordered cubic mesoporous FDU- 12

The FDU- 12 synthesis was based on an adjusted protocol described previously in reference 14. F127 (2.0 g) and KCl (5.0 g) were dissolved in 120 mL of 2 mol L^{-1} HCl. The mixture was stirred at 15 °C using mechanical and magnetic apparatus until visually transparent (~ 5 min). The 2.6 mL of TMB (2.0 g, (1:1) w/w of TMB) was added to the polymer solution by two processes (Table 1): (i) together with TEOS, just after the polymer dissolution, keeping the solution under stirring for 24 h (named SA, simultaneous addition of TEOS and TMB), (ii) immediately after the polymer dissolution, kept under constant stirring by 2 h, when 8.6 mL (9.2 g) of TEOS was added, also kept under stirring for 24 h (named A2, addition of TEOS after 2 h). Both solutions were put inside Teflon® autoclaves and left at 60, 80, 100, 120, and 140 °C with air circulation for 24 h to perform the hydrothermal treatment. The autoclaves are hermetically sealed with an aluminum cap and heated under controlled temperature in a conventional furnace. Then, the material was filtered, washed with water, and dried at 60 °C. The dried solid was calcined under controlled conditions at a

Table 1 Synthesis conditions

Sample	TMB/TEOS (w/w)	Addition TMB/TEOS	Hydrothermal temperature (°C)	Vessel Cover	Type of stirring
FD60SAPC	1:1	Simultaneous	60	Parafilm Cover (PC)	Mechanical/Magnetic
FD80SAPC	1:1	Simultaneous	80	Parafilm Cover (PC)	Mechanical/Magnetic
FD100SAPC	1:1	Simultaneous	100	Parafilm Cover (PC)	Mechanical/Magnetic
FD120SAPC	1:1	Simultaneous	120	Parafilm Cover (PC)	Mechanical/Magnetic
FD140SAPC	1:1	Simultaneous	140	Parafilm Cover (PC)	Mechanical/Magnetic
FD60 A2PC	1:1	TEOS after 2 h	60	Parafilm Cover (PC)	Mechanical/Magnetic
FD80 A2PC	1:1	TEOS after 2 h	80	Parafilm Cover (PC)	Mechanical/Magnetic
FD100 A2PC	1:1	TEOS after 2 h	100	Parafilm Cover (PC)	Mechanical/Magnetic
FD120 A2PC	1:1	TEOS after 2 h	120	Parafilm Cover (PC)	Mechanical/Magnetic
FD140 A2PC	1:1	TEOS after 2 h	140	Parafilm Cover (PC)	Mechanical/Magnetic
FD100 A2PC	2:1	TEOS after 2 h	100	Parafilm Cover (PC)	Mechanical/Magnetic
FD140 A2PC	2:1	TEOS after 2 h	140	Parafilm Cover (PC)	Mechanical/Magnetic
FD100 A2PC	4:1	TEOS after 2 h	100	Parafilm Cover (PC)	Mechanical/Magnetic
FD140 A2PC	4:1	TEOS after 2 h	140	Parafilm Cover (PC)	Mechanical/Magnetic
FD100 A2PL	4:1	TEOS after 2 h	100	Plastic Lid (PL)	Magnetic
FD140 A2PL	4:1	TEOS after 2 h	140	Plastic Lid (PL)	Magnetic
FD100 A2GL	4:1	TEOS after 2 h	100	Glass Lid (GL)	Mechanical/Magnetic
FD140 A2GL	4:1	TEOS after 2 h	140	Glass Lid (GL)	Mechanical/Magnetic

SA Simultaneous Addition of TMB and TEOS, *A2* Addition of TEOS 2 h after F127 + TMB

heating rate of 2 °C.min^{-1} from room temperature to 540 °C under N_2 atmosphere, and then switched to air, maintaining an isotherm for a period of 5 h.

The temperatures of 100 °C and 140 °C were chosen for the other synthesis conditions, where the amounts of TMB were adjusted to the following proportions: (2:1) and (4:1), wt.%. TEOS was added after 2 h of mixing F127 and TMB (condition A2).

All synthesis conditions are shown in Table 1.

2.3 Enzyme encapsulation

Papain (PPN) was dissolved in deionized water, and this solution was added to the silica samples, SS (FD100 A2GL and FD140 A2GL), at a weight ratio of 1SS:0.3PPN:33H_2O. Before the addition of papain, the silica samples were activated at 200 °C to remove adsorbed water. The dispersions (PPN, water, and silicas, pH = 5.3) were stirred for 60 min at room temperature, and the resulting material was placed in a freezer at − 25 ± 5 °C for 24 h. The frozen samples were then lyophilized for 48 h (two days) at − 52 °C under vacuum (35 µmHg) using a Liobras freeze-dryer (model Liotop® L108, São Carlos, Brazil). The resulting samples were referred to as FD100:PPN and FD140:PPN, where FD100 is FD100 A2GL and FD140 is FD100 A2GL, related to the synthesis of FDU- 12 using a hydrothermal treatment temperature of 100 and 140 °C, respectively (4:1 is the mass ratio TMB:F127), A2 represents the addition of TEOS 2 h after F127 + TMB, GL = glass Lid, and PPN is papain.

2.4 Enzyme activity assay

The proteolytic activity of papain was determined by a spectrophotometric method by measuring the rate at which p-nitroaniline was released at 405 nm. p-nitroaniline, a yellow substance, was produced by the hydrolysis reaction of Na-benzoyl-DL-arginine p-nitroanilide hydrochloride (BAPA) (Sigma-Aldrich®, USA), a specific substrate for proteolytic enzymes as papain. An analytical curve was built to quantify papain activity by relating the rates of BAPA conversion to the concentrations of papain.

The rates of BAPA conversion were determined through the relationship between the absorbance at 405 nm of the BAPA hydrolysis reaction product and reaction time (zero, 15, 30, and 45 min) for eight different papain concentrations. Initially, solutions of BAPA (880 µg mL^{-1}), acetic acid (30% v/v), and cysteine-phosphate buffer (pH 6.8) containing papain ranging from 0.010 to 0.350 mg mL^{-1} were prepared for immediate use.

For the test, one 96-well plate was prepared with reagents in an ice-bath to prevent the reaction from starting prematurely. Each well contained 125 µL of BAPA solution and 100 µL of papain solutions at different concentrations for the four reaction times. For the wells related to the zero-time reaction, 50 µL of acetic acid was added before the

plate was placed in a heated bath at 40 °C, and the reaction time started. Acetic acid solution (50 µL) was also added to the corresponding wells at 15, 30, and 45 min to stop the reaction. The same plate was used to read the BAPA reaction product in a spectrophotometer at λ = 405 nm on a Synergy HT microplate reader (Biotek Instruments, USA). The absorbance values were recorded and related to reaction time, making it possible to determine the rate of BAPA conversion for each papain concentration. The linear relation between the rates of BAPA conversion and papain concentration allows the determination of the equivalent active papain concentration in a sample with an unknown enzyme concentration.

The tests for FD100:PPN and FD140:PPN composites were performed by weighing the amount of each composite necessary to reach 1.0 mg papain in the composite. Thus, 4.3 mg of each composite was weighed and dispersed in 4 mL of cysteine-phosphate buffer (pH 6.8), resulting in a nominal papain concentration of 0.25 mg mL^{-1}. These dispersions were directly used to evaluate papain activity using the BAPA substrate-specific method. For this, 100 µL of dispersions were taken immediately after homogenization and transferred to a 96-well plate. The experiment followed the procedure used to build the analytical curve for papain activity. The theoretical concentration of PPN in each well was 0.09 mg mL^{-1}. All the experiments were done in triplicate. The BAPA conversion rates for the reaction products were determined by the relation between the absorbance of the reaction products at 405.

2.5 Leaching test of encapsulated papain on the FDU- 12 samples

The leaching test was performed under stirring in aqueous solution. For this, 4.0 mg of the composites (FD100:PPN and FD140:PPN) were weighed and dispersed in 10 mL phosphate-buffered saline (PBS) 20 mM pH 6.8 in glass bottles. The dispersions were kept under magnetic stirring for 1, 2, 4, and 8 h at room temperature. The dispersions were filtered in a nylon membrane (0.22 µm pore) discarding the first 4.0 mL for filter saturation. The next 4.0 mL filtered were collected and analyzed in a spectrophotometer (Thermo, Evolution 201, Brazil) in the wavelength range from 200 to 400 nm. A pristine silica sample was used as a blank for the measurements. The baseline was obtained in the same buffer. The pH of the filtered samples was measured after the leaching assays. All analyses were done in triplicate. The data of absorbance were applied in an analytical curve for PPN in PBS ranging from 0.040 to 0.800 mg mL^{-1}, obtained as described by Nambu et al. [21] for determination of the PPN concentration, allowing to estimate the amount of PPN leached with time. The data obtained were compared to using One-Way ANOVA at a level of significance of 0.05.

2.6 Methods of characterization

All samples were characterized by Small Angle X-ray Scattering (SAXS). The experiments were performed in the laboratory-based SAXS equipment, Xenocs-XEUSS™, located at the Institute of Physics, University of São Paulo, Brazil. This set-up has a microfocus X-ray source Genix and copper anode, λ = 1.5418 Å. Two scatter slits collimate the beam that reaches the sample with a square cross-section of 0.5 mm × 0.5 mm. The primary and scattered beams remain in a vacuum chamber to avoid scattering by the air. The sample is placed between two mica foils. The two-dimensional scattering patterns were registered by a Pilatus 300 K, 20 Hz detector system (from Dectris). The scattering curves were obtained after one hour of exposure time. The images were integrated with the Fit2D software [22]. The data treatment, blank subtraction, and data normalization were performed with the program package SUPERSAXS [23]. The blank (synthetic ester oil) was independently measured and subtracted from the sample data. The lattice parameter was determined using the first and intense (111) diffraction peak.

Nitrogen adsorption/desorption isotherms (NAI) were measured with a Micromeritics ASAP 2020 volumetric adsorption analyzer using nitrogen of 99.998% purity. Measurements were performed in the range of relative pressure from 10^{-6} to 0.99 liquid nitrogen on the samples degassed for 2 h, under a vacuum of about 10^{-3} Torr, at 200 °C. The specific surface area was evaluated using the BET (Brunauer–Emmett–Teller) method [24]. The total pore volume was estimated from the amount adsorbed at the relative pressure of 0.99. The micropore volume, V_{mi}, was evaluated using the α plot method in the standard reduced adsorption range from 1.0–1.4. The pore size distribution (PSD) was calculated using Kruk, Jaroniec, and Sayari (KJS) method [25].

Scanning electronic microscopy (SEM) images were recorded on a JEOL field emission electron microscope, model JSM 6701-F, operating with a secondary electron imaging (SEI) detector. The samples were placed onto conductive double-sided adhesive carbon tape and were analyzed without any coating.

Transmission electron microscopy (TEM) was used to verify the structure of ordered cubic mesoporous FDU- 12. The sample was dispersed in isopropyl alcohol and put onto a collodion film on a 400 mesh Cu grid. The dried samples were analyzed in a JEM- 2100 Jeol transmission electron microscope, operating at 200 kV.

Differential scanning calorimetry (DSC) and thermogravimetric analysis (TGA) measurements were performed using a simultaneous thermal analyzer DSC/TGA, the Discovery SDT 650 from TA Instruments. DSC/TGA curves were obtained at a heating rate of 10 °C min^{-1}, in the temperature range from 35 to 900 °C, under a dynamic air

atmosphere (100 mL min^{-1}), using alumina crucible with ca. 5 mg of the sample mass. The experimental percentage of papain in the composites was estimated based on the weight loss observed in the 2nd and 3rd stages of the thermogravimetric curves (Table S1).

Transform infrared spectroscopy (FTIR) spectra were recorded on an IRPrestige- 21 FTIR spectrometer (Shimadzu Corp, Kyoto, Japan) in the wavenumber range from 4000 to 400 cm^{-1}, employing a resolution of 4.0 cm^{-1} and an average of 256 scans, using a diffuse reflectance (model DRS- 8000 A) accessory. To establish the background, potassium bromide (KBr) powder was utilized, and a small amount, approximately 5% (w/w) of the sample, was added for analysis.

3 Results and discussion

3.1 . Time of TEOS and swelling agent addition

Figure 1a–b and Fig. 2a–b, representing cases (i) and (ii) respectively, described above, revealed that samples

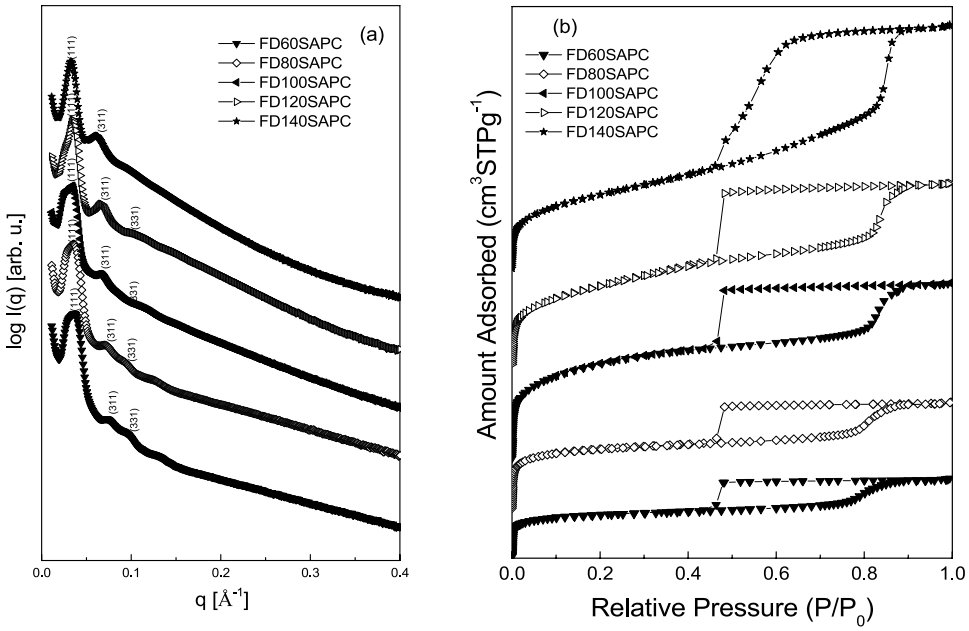

Fig. 1 **a** SAXS of samples synthesized with simultaneous addition of TMB and TEOS (SA) and **b** nitrogen isotherms of samples synthesized with simultaneous addition of TMB and TEOS (SA)

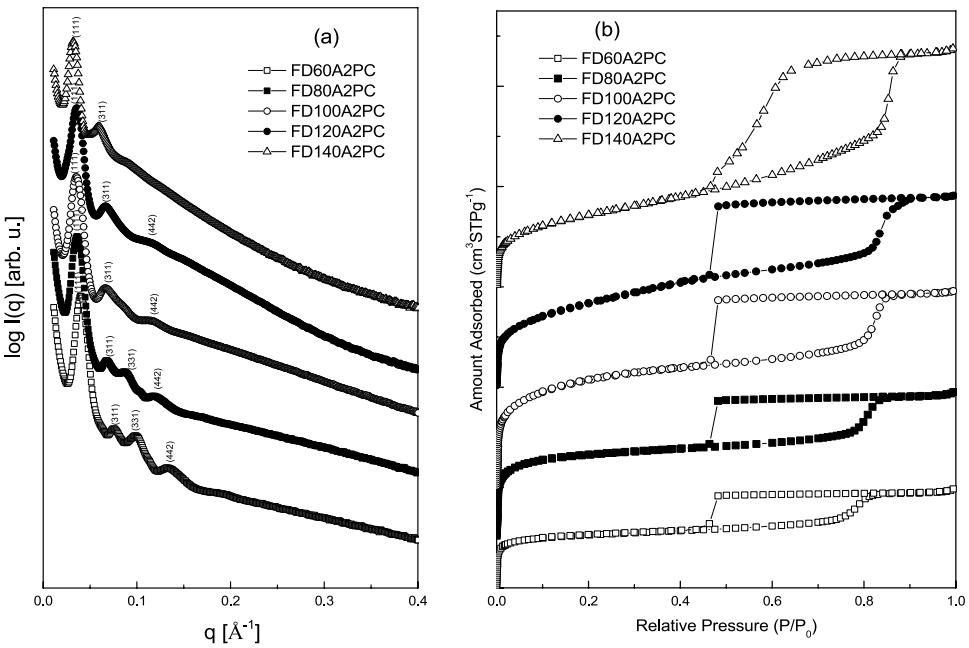

Fig. 2 **a** SAXS of samples synthesized with the addition of TEOS after two hours of TMB inclusion (A2) and **b** nitrogen isotherms of samples synthesized with the addition of TEOS after two hours of TMB inclusion (A2)

synthesized at lower hydrothermal temperature (HT) presented several diffraction peaks, the number of which decreased with increasing HT. Table S2 presents the indexed peaks of the FDU- 12 structure for al samples. As can be observed, the obtained structures of FD60SA, FD60 A2, FD80SA, FD80 A2, FD100SA, FD100 A2 have indexed reflections (111), (311), (400), (331) and (442). The FD120SA and FD120 A2 samples presented peaks indexed as (111), (311), (400), and (331). Finally, FD140SA and FD140 A2 samples showed characteristic peaks that can be attributed to the indexed reflections (111), (311) and (400). All samples presented an ordered cubic mesoporous structure with *Fm3 m* symmetry. The results show that a broader dispersion of lattice parameters occurs when simultaneous additions (SA) of TMB and TEOS are used, as well as this behavior is more accentuated in the syntheses at low temperatures (≤ 100 °C). This finding shows that a better structure matrix is obtained with the process where TEOS is added after 2 h from the introduction of F127 and TMB to the synthesis solution.

Also to check the influence of TMB/template ratio and temperature on the OMS properties, two other groups of samples were prepared with TMB/template ratios (2:1) and (4:1), at 100 and 140 °C, prepared with A2 condition. Table S2 evidenced that the increase in temperature is responsible for the more disordered porous structure. No substantial variations were detected in peak shape or intensities from the SAXS results. In this case, more pronounced differences in these two sets of samples are evidenced by the N_2 adsorption/desorption results, as will be discussed below.

Furthermore, three different ways to isolate the reactors in order to avoid evaporation and to check the influence of the stirring procedure were performed. Initially, a parafilm cover (PC) was used, with magnetic and mechanical stirring, which do not perfectly seal the reaction vessel. After, a plastic lid (PL) with magnetic stirring, and finally, a new glass lid reactor (NR) was used with magnetic and mechanical stirring. Table S2 presents the SAXS indexed peaks at the above-mentioned conditions. Only a slight decrease in peak width, characteristics of a more ordered porous structure, was observed by using the plastic lid (PL) compared with the parafilm cover (PC), and no detectable differences by using the glass lid (GL).

Figure 1b and Fig. 2b show the results of N_2 adsorption/desorption curves for two groups of samples, both synthesized at temperatures of 60, 80, 100, 120, and 140 °C for SA and A2 conditions, respectively. These synthesis procedures were carried out in a reactor covered with parafilm and under magnetic and mechanical stirring. The pore size distributions in adsorption and desorption are presented in Supplementary Information (FigureS1 and S2).

The hysteresis loop observed for the samples is typical for ordered mesoporous silica with a cubic cage-like structure, distorted for the synthesis at 140 °C. The BET surface area (S_{BET}), external surface area (S_{ext}), mesopore volume (V_{MP}), micropore volume (V_{mp}), internal pore size (W_p), entrance pore size (w_p) and lattice parameter (a) allow to determine how temperature, swelling agent concentration and synthesis process affect the textural and structural properties of FDU- 12. Tables 2 and 3 present the textural and structural parameters obtained for all analyzed samples. In this case the S_{BET} presents a maximum value for the HT at 100 °C for both syntheses conditions, SA and A2. In this case it is possible to associate the decrease of S_{BET} for higher temperature to a decrease of micropore volume, as already reported by Matos et al. [26]. Also it is possible to observe in Table 3 that the proper isolation of the synthesis vessel contributes to increase S_{BET}, since all the solution components were not lost to external medium, as well as the mechanic and magnetic stirring are recommended to homogenize the liquid solution. Comparing the results with the two different TMB:F127 wt% ratio, 2:1 and 4:1, it is clear that the increase

Table 2 Textural and structural parameters obtained from N_2 sorption and SAXS analysis. TMB:F127 wt% was equal 1:1. Samples synthesized at different temperature and TEOS addition time

Samples	S_{BET} (m^2g^{-1})	S_{ext} (m^2g^{-1})	V_{MP} (cm^3g^{-1})	V_{mp} (cm^3g^{-1})	W_p (nm)	w_p (nm)	a (nm)
FD60SAPC	314	71	0.11	0.10	10.7	4.68	29.8
FD80SAPC	444	87	0.13	0.15	11.7	4.68	30.5
FD100SAPC	735	137	0.24	0.26	13.2	4.68	31.5–41.2
FD120SAPC	606	207	0.44	0.18	13.3	4.68	31.2
FD140SAPC	571	462	0.88	0	14.8	4.68–5.47	33.6
FD60 A2PC	366	92	0.13	0.11	11.8	4.40	27.4
FD80 A2PC	576	114	0.16	0.19	11.8	4.68	30.5
FD100 A2PC	764	160	0.25	0.26	12.9	4.68	30.5
FD120 A2PC	528	191	0.42	0.14	12.9	4.68	30.5
FD140 A2PC	517	407	0.81	0	15.0	4.68–5.74	33.6

SA Simultaneous Addition of TMB and TEOS, *A2* Addition of TEOS 2 h after F127 + TMB, *PC* Parafilm Cover. S_{BET} Surface area, S_{ext} External surface area, V_{MP} Mesopore volume, V_{mp} Micropore volume, W_p Mesopore diameter, w_p Entrance pore diameter, a = Lattice parameter

Table 3 Textural and structural parameters obtained from N_2 sorption and SAXS analysis. TMB:F127 wt% was varied and hydrothermal treatment temperature

Samples	S_{BET} (m^2g^{-1})	S_{ext} (m^2g^{-1})	V_{MP} (cm^3g^{-1}) (BJH)	V_{mp} (cm^3g^{-1}) (BJH)	W_p (nm)	w_p (nm)	a (nm)
FD100 C(2:1)A2PC	697	435	0.47	0.45	13.4	4.70	34.3
FD140 C(2:1)A2PC	667	134	0.23	0.24	16.9	4.68–7.53	38.3
FD100 C(4:1)A2PC	679	734	0.83	0.16	14.4	4.69	42.4
FD140 C(4:1)A2PC	734	117	0.20	0.29	20.4	4.68–7.67	46.4
FD100 C(4:1)A2PL	932	451	0.70	0.17	13.0	4.40	46.9
FD140 C(4:1)A2PL	368	389	0.81	0.00	22.7	4.68–8.72	43.0
FD100 C(4:1)A2GL	1041	181	0.41	0.38	17.1	4.64	42.4
FD140 C(4:1)A2GL	574	458	1.31	0.00	22.4	8.79	45.0

A2 Addition of TEOS 2 h after F127 + TMB, *PC* Parafilm Cover, *PL* Plastic Lid, *GL* Glass Lid. S_{BET} Surface area, S_{ext} External surface area, V_{MP} Mesopore volume, V_{mp} Micropore volume, W_p Mesopore diameter, w_p Entrance pore diameter, a Lattice parameter

in this ratio responds for the increase in S_{BET}, V_{MP} and W_P as well as to promote entrance pores with different sizes.

S_{ext}, V_{MP} and W_p increase with increasing temperature in the range of 60–140 °C. The V_{mp} increases in the temperature range of 60–100 °C and it decreases in the temperature range of 120—140 °C, showing the densification of the silica walls. The pore entrance size remains at approximately 4.7 nm in the range of 60–120 °C and at 140 °C the pore entrance size presents a bimodal characteristic with entrance pore diameters at 4.7 nm and 5.7 nm, which demonstrated that different amounts of the swelling agent were inside the polymer F127 micelles. The results point out that the increase in the hydrothermal temperature contributes to enhancing the mesoporosity of FDU- 12, but with the decrease in the porous ordered domains. The pore diameter is tuned by the hydrothermal treatment as pointed out by other authors [15], and morphology of the silica particles is susceptible to the stirring rate [27]. In current study it was observed that the textural properties are slightly improved with the addition of TEOS after 2 h of the addition of the TMB pore swelling agent.

Figure 3 shows micrographs of the synthesized material. Large macropores and dense silica walls are observed in the TEM images. Also, it is possible to visualize the cubic ordered mesoporosity, having dimensions compatible with the N_2 sorption results. The material prepared with simultaneous addition of TEOS and TMB presents, besides different lattice parameters, inclusions of hexagonal ordered structure, as can be detected by TEM and SAXS (Fig. S3).

Figure 4 shows the thermogravimetric, derivative thermogravimetry and differential scanning calorimetry curves of the papain and the composites (FD100:PPN and FD140:PPN). The TGA, DTG and DSC curves for pristine silicas are shown in Fig. S4.

The papain exhibits three steps of weight loss, as observed in the TG curves, which are associated with five peaks in the DTG curves. The first step occurs between room temperature and 140 °C, corresponding to water elimination

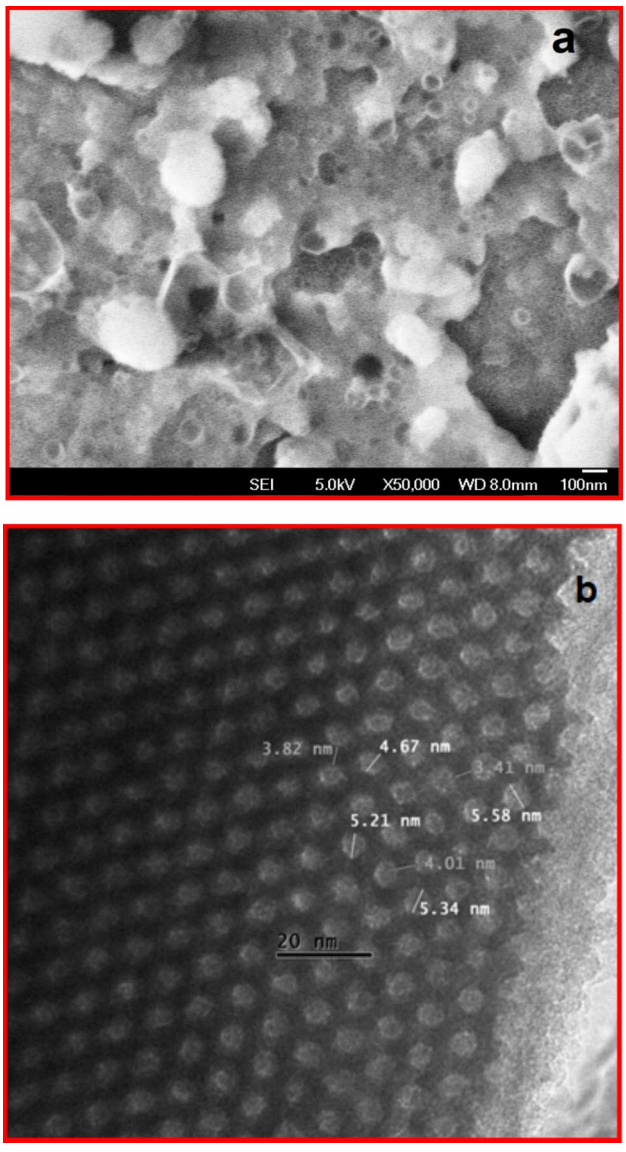

Fig. 3 **a** SEM and **b** TEM images of FDU100SA sample, synthesized with TMB:F127, 1:1 wt%

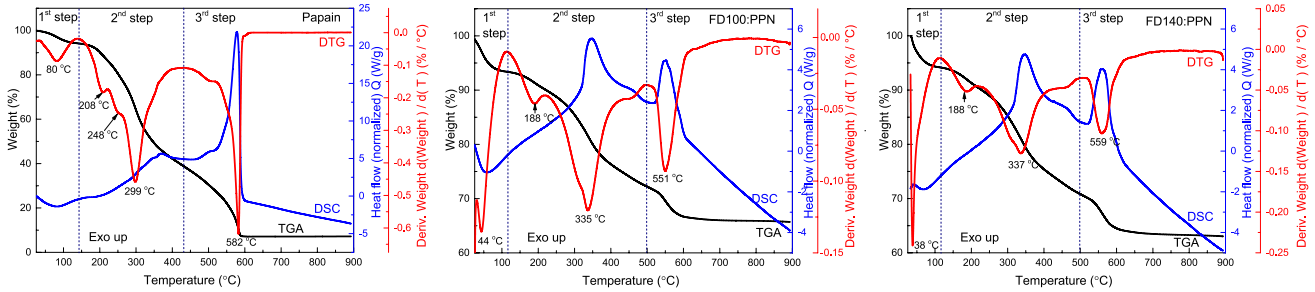

Fig. 4 TG and DSC curves of papain and the FD100:PPN and FD140:PPN composites

(5.8%), with a DTG peak at 80 °C and a corresponding endothermic peak in the DSC curves. The subsequent steps are attributed to papain degradation, which occurs within the temperature ranges of 140 °C to 430 °C and 430 °C to 900 °C. These degradation steps are characterized by consecutive mass losses, with one process initiating before the completion of the previous one, as evidenced by the multiple peaks observed in the DTG curves. The degradation processes are accompanied by energy release, as indicated by two distinct exothermic events observed in the DSC curve. The prominent DSC peak, observed at 575 °C, is particularly intense and corresponds to the release of carbonaceous materials, which occurs under a synthetic air atmosphere.

The TG curves (Fig. S4) of silica samples display two distinct steps of weight loss. The first step, occurring from room temperature to 170 °C, is assigned to water elimination, with a weight of approximately 15% for the FD100 sample and 9% for the FD140 sample. The second step, occurring between 170 and 900 °C, is attributed to silanol elimination, with weight losses of approximately 3% and 2%, respectively (Table S1). The water elimination corresponds to an endothermic peak, while the silanol elimination is associated with an exothermic process, as observed in the DSC curves. The latter displays a broad band in the temperature range of 170 to 900 °C, with a maximum around 400 °C.

The TG curves of the composites present a profile similar to that of pure papain. However, the onset temperature of the composites (Table S1) is lower than that of papain, which can be attributed to changes in papain crystallinity. Since the composites were lyophilized, this process likely influenced the crystallite size. Considering the weight ratio of 1SS:0.3PPN:33H_2O for the composites, the nominal papain content is 23%. By TGA analysis (Table S1), the second (from 115 to 500 °C) and third (from 500 to 900 °C) steps of weight loss in the composites are assigned to papain degradation and silanol elimination, corresponding to approximately 28% and 30% for FD100:PPN and FD140:PPN, respectively. Considering the silanol group concentration (approximately 2–3 mmol.g^{-1}), the experimental papain content in the composites is estimated to be around 25% for FD100:PPN and 27% for FD140:PPN.. Notably, these experimental values are higher than the nominal content, a discrepancy that may be related to silica loss during the transfer process to the container where the papain was incorporated. Due to extremely fine powder, some material may have been lost during this step. The complete data are presented in supplementary Table S1.

From the DTG curves of the composites, it is observed that papain degradation, which occurs between 115 and 900 °C, exhibits peaks with similar profiles among the composites, but with slightly different values compared to pure papain. The same trend is observed in the exothermic peaks in the DSC curves. When comparing the DSC curves of pure papain and the composites, significant changes in the intensity of the peaks are evident. For pure papain, the last peak, observed around 580 °C, is more intense than the penultimate peak, which appears around 299 °C. In contrast, the corresponding peaks of composites, approximately 335 °C for the penultimate and 550 °C for the last, exhibit similar intensities for the composites. These alterations in the DTG and DSC profile of the composites may be related to changes in papain crystallinity, likely caused by the lyophilization process and the incorporation of papain into the mesopores of the silica matrix.

The FTIR spectra shown in Fig. 5 confirm the presence of papain in both composites (FD100:PPN and FD140:PPN), corroborating the TGA analysis.

The FTIR spectra of pristine silicas (Fig. 5) exhibit a broad band ranging from 3050 to 3600 cm^{-1}, corresponding to the stretching vibration of hydroxyl groups (νOH) in silanol groups (Si–OH) and adsorbed water. The OH bending vibration of physically adsorbed water molecules is observed at 1623 cm^{-1}. The prominent band at 1080 cm^{-1} and the vibrational band at 450 cm^{-1} are assigned to the asymmetric stretching and bending vibrations of siloxane groups (Si–O–Si), respectively. Additionally, a symmetric stretching band from SiO bonds is shown around 800 cm^{-1}. Notably, only the FD140 sample displays the band of free silanol groups at 3737 cm^{-1}.

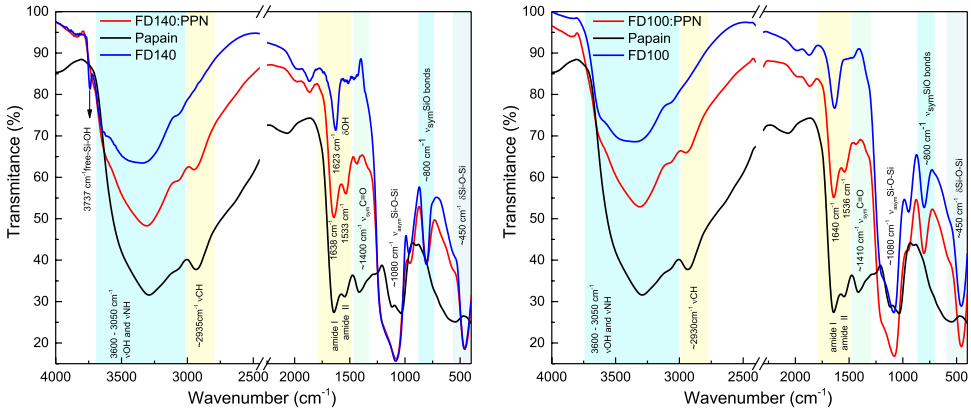

Fig. 5 FTIR spectra of papain, pure silicas (FD100 and FD140) and FD100:PPN and FD140:PPN composites

In the spectra (Fig. 5) of the composites (FD100:PPN and FD140:PPN), all silica bands are evident, except for the band corresponding to free silanol groups that appeared in the pristine FD140 at 3737 cm^{-1}. The absence of this band in the FD140:PPN composite suggests a strong interaction between papain and silica. The NH stretching band, around 3050 cm^{-1}, coincides with the broad absorption band of OH. Additional papain bands are observed at 2930 cm^{-1}, attributed to CH_2 stretching, and at 1640 cm^{-1} and 1535 cm^{-1}, corresponding to the vibrations of amide I and amide II bands, respectively. The band around 1400 cm^{-1} is attributed to C = O symmetric stretching.

Finally, the samples of FD100:PPN and FD140:PPN were analyzed by laser diffraction for characterization of the size particle distribution. The samples were dispersed in water and poured into the equipment chamber analysis until obscuration upper than 10. Particle size distribution values are shown in Table 4 for both composites with PPN. The mean diameter for FD100:PPN expressed in volume of the particles (D_{mv}) was 23.91 ± 0.02 µm, around 15% larger than for FD140:PPN (20.76 ± 0.02 µm), whereas the mean diameter expressed in number of the particles (D_{mn}) was 2.66 ± 0.02 µm and 3.60 ± 0.01 µm, respectively.

The measures of mean diameter and its fractions in 10, 50 and 90% of particles populations (D10, D50 and D90) allowing to calculate the dispersity (SPAM) and uniformity ratio (UR) as index of uniformity of size distribution since a closer to 1.0 the values as uniform the particle size. Thus, comparing the composites containing PPN, the FD140:PPN showed the best particle size uniformity (SPAM = 1.78 ± 0.00; UR = 5.77 ± 0.01), showing that temperature might interfere with size distribution and uniformity.

3.2 . Papain activity and desorption from silica-papain composites

In this work, papain was associated with FDU- 12 mesoporous silica synthesized in temperatures 100 and 140 °C, resulting in the samples FD100:PPN and FD140:PPN, respectively. PPN biological activity was evaluated by converting BAPA, a specific substrate for the enzyme, followed by the increase in absorbance at 405 nm. Hence, the analytical curve for papain activity was obtained ranging the enzyme concentration from 0.0036 to 0.1273 $mg.mL^{-1}$ in a 96-well plate. The BAPA conversion rates were obtained for each papain concentration, the analytical curve was built, and the best fit was obtained with $r^2 = 0.9841$, for the equation: BAPA conversion rate = 0.16066 [PPN] ± 0.00004 (Fig. S5).

The analyses of PPN activity in the composite samples were carried out at the same conditions used in the analytical curve. The composites containing PPN (FD140:PPN and FD100:PPN) were dispersed in PBS pH 6.8, diluted up to 0.073 $mg.mL^{-1}$ PPN, and left to react with BAPA. The analysis unveiled that PPN keeps the catalytic activity even after all procedures to prepare the composites with mesoporous

Table 4 Particle size distribution by laser diffraction analysis (n = 3), using purified water as dispersion medium of the composites

Sample	D10v (µm)	D50v (µm)	D90v (µm)	SPAMv*	Dmv (µm)	Dmn (µm)	UR**
FD140:PPN	6.55 ± 0.03	18.05 ± 0.02	38.65 ± 0.03	1.78 ± 0.00	20.76 ± 0.02	3.60 ± 0.01	5.77 ± 0.01
FD100:PPN	5.97 ± 0.04	21.15 ± 0.04	45.59 ± 0.07	1.87 ± 0.01	23.91 ± 0.02	2.66 ± 0.02	8.98 ± 0.07

*SPAMv: (D90-D10)/d50: dispersity of particle size–values lower than 2.0 are considered adequate and suggest a normal particle size distribution

**UR Dmv/Dmn: Uniformity Ratio, Values between 1 and 5 suggest a more uniform size distribution, whereas values over 10 indicate a polydisperse granulometric distribution

silica. Besides, for FD140:PPN, the papain activity was 5.86% larger than the theoretical value of PPN concentration in the composite (23%w/w), or that determined in thermogravimetric analysis in the second step of mass loss, 23.4%w/w (Table S1). The value of 105.86% indicates that FD140RN silica did not impair the enzyme activity or the substrate access to reach enzyme molecules entrapped in the mesopores of the silica, allowing the interaction between them, resulting in BAPA conversion.

On the other hand, the PPN associated with FD100 resulted in a superior papain activity, 41.89% larger than the expected for the PPN concentration in the sample determined by thermogravimetric analysis (21.2%w/w) and 34.04% higher than found in FD140. This result suggests that the association of FD100 and PPN can provide a gain in the enzyme activity caused by the easy access to the enzyme molecules inside the mesopores, or due to the release of PPN from silica mesopores to the medium. In fact, the greater ratio between S_{ext}/S_{BET} for FD100 unveils that around 80% of the silica surface is related to the internal porosity, instead of 21% for FD140 S_{ext}/S_{BET}, consequently, a larger efflux of medium containing BAPA is possible in FD100, favoring the substrate reaching the enzyme. Furthermore, the microporosity present in FD100 suggests the presence of uncountable pathways through the silica particles which drive BAPA molecules to the mesoporosity inside silica where PPN might be hosted and protected, which might contribute to activity gain. Besides, as demonstrated by FTIR (Fig 5), there are no free silanol groups in FD100, suggesting that PPN inside silica mesopores could be more untied, with a lower number of interactions silica – PPN, being free to interact and convert BAPA in a side, and for leaching from the silica mesoporous, becoming the enzyme available in the medium to interact with the specific substrate.

Matsuura et al. [28] observed an increase in the trypsin activity when that enzyme and lipase were co-encapsulated mesoporous silica. The improvement in trypsin activity was attributed to a reduction in self-digestion since it is a proteolytic enzyme. On the other hand, in our previous findings [29] the association of PPN with SBA- 15 resulted in a 15% decrease on enzyme activity compared to free PPN, demonstrating that the cubic matrix is more suitable for catalytic applications with papain.

The importance of encapsulation process to achieve more stability and, in the case of immobilization, reusable enzymes, in silica matrices, was already emphasized [30], showing interest in the issues addressed in the present research.

However, despite the PPN catalytic activity found using BAPA as a specific substrate, it is important to note that BAPA is a low molecular weight compound, able to permeate through the silica microporous when dispersed in an aqueous medium, and consequently, becoming favorable to the interaction substrate-enzyme. Dissimilar, larger molecules like proteins or the enzyme interaction with tissues might be impaired if the PPN was immobilized into the silica porous and the narrow and meshing paths in which the enzyme is kept. Thus, for therapeutic uses it is important to guarantee that PPN associated with FD100 and FD140 is released from the silica's micro and mesoporosity to the medium, aiming to play the catalytic role. To demonstrate this, composites of FD100 or FD140 and PPN were submitted to a leaching test in which free PPN in the medium was monitored directly by spectrophotometry at 230 nm.

Hence, an analytical curve of PPN in PBS 20 mM pH 6.8 was built in the range from 0.04 to 0.80 mg.mL- 1, resulting in $r^2 = 0.9994$ for the best fit, whose linear equation was: Absorbance = 2.8418[PPN]–0.0381. The profiles of PPN desorption from the silica composites are shown in Fig 6. The profiles unveiled that for both composites the PPN rapidly desorbs, releasing about 85% and 50% of PPN from FD100:PPN and FD140: PPN, respectively, in the first hour.

This fast and large PPN release in the first hour from FD100:PPN is in accordance with the greater internal

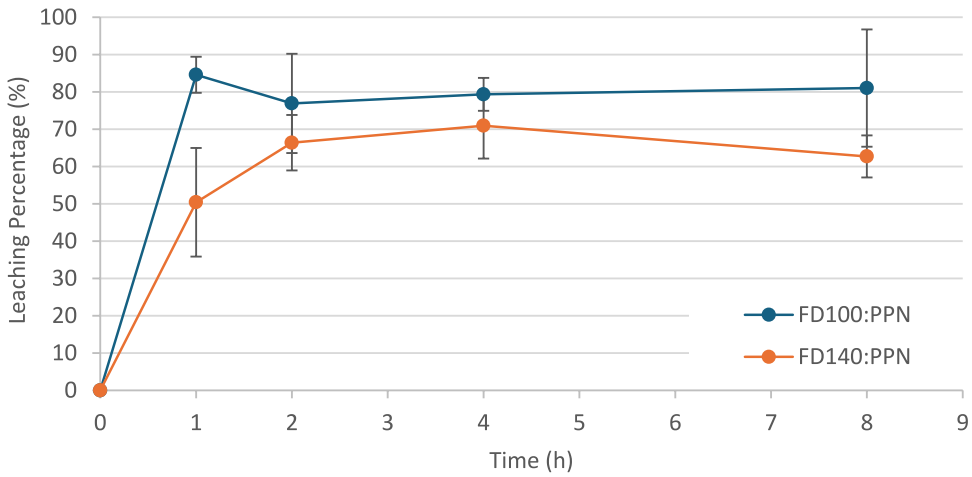

Fig. 6 Leaching of PPN from FD10 and FD140 composites in purified water under magnetic stirring at room temperature

surface obtained for this composite as demonstrated before. The superior area might allow PPN to get the best dispersion into the silica pores, therefore the enzyme might be more available to dissolve and react with BAPA, resulting in higher rates of BAPA conversion, understood as higher biological activity. It is important to note that the percentage of PPN leaching over the 8 h test was practically constant, suggesting part of PPN might have been immobilized in FD100 silica, which can extend the PPN activity, enhancing, in some cases, the interest in exploring this kind of composite for therapeutic and industrial aims. Unlike, FD140:PPN showed a less intense release of PPN in the first hour reaching 50% of PPN and 71% only after 4 h, suggesting that the lesser internal surface might lead PPN to adsorb and agglomerate onto the external surface, taking more time for dissolution and leaching to the PBS medium. Further, more restricted micro and mesoporous in this silica might result in more intense entrapment, keeping about 30% of PPN inside the silica pores.

4 Conclusion

This work reports on the importance of controlling the syntheses environment, as well as the influence of time inclusion of chemical compounds inside the reaction vessel. The SAXS results demonstrated that a better structure matrix, represented by a homogeneous lattice parameter, is obtained when TEOS is added after 2 h from the introduction of homogenized F127 and TMB to the acidic solution. This result is corroborated by the better textural properties obtained by nitrogen adsorption/desorption data for the same synthesis procedure. The hydrophobic characteristics of TMB induce its entrance in the F127 micelles, making an improved liquid crystalline order. Other important synthesis protocol, determined by the analysis of different methods of covering the reaction vessel, revealed that it is demanding to seal the system in order to preserve all compounds in its proper concentration. Also, the investigated temperature of the HT in a closed autoclave is responsible for the increase on the pores sizes, as well to the rise of disorder with HT increase. The high TMB concentration contributes to enhance in surface area, mesopore volume and size, being an important factor to tailor the material properties for specific applications. All the characterization on the yield of papain internalization inside the silica macro and mesoporosity revealed its integrity and a fast release at the first hour, with a continuous and slow liberation with time. An activity increase of almost 42%, much better than previous studies using SBA- 15 hexagonal ordered mesoporous silica, was verified for HT at 100 °C, which is the best HT temperature detailed in this study.

Supplementary Information The online version contains supplementary material available at https://doi.org/10.1007/s10934-025-01801-1.

Acknowledgements This study is part of the National Institute of Science and Technology in Pharmaceutical Nanotechnology: a transdisciplinary approach INCT-NANOFARMA, which is supported by São Paulo Research Foundation (FAPESP, Brazil) Grant #2014/50928 - 2, and by ''Conselho Nacional de Desenvolvimento Científico e Tecnológico'' (CNPq, Brazil) Grant # 465687/2014 - 8, and by "Fundação Coordenação de Aperfeiçoamento de Pessoal de Nível Superior" (CAPES, Brazil), Grant # 88887.358273/2019 - 00. Thanks are due to São Paulo Research Foundation (FAPESP, Brazil) for Grants 2017/17844 - 8, 2019/07007 - 7 and 2019/08582 - 5.

Author contributions L.C. C.S conceptualization, carried out experiments, wrote the main manuscript text, prepared figures, D.W. Losito carried out experiments, D.R.O. Pimentel carried out experiments, N. Andreo-Filho conceptualization, carried out experiments, wrote the main manuscript text, prepared figures, T.S. Martins conceptualization, carried out experiments, wrote the main manuscript text, prepared figures, L. Otubo carried out experiments, O.A. Sant´Anna conceptualization, M.C.A. Fantini wrote the main manuscript text, prepared figures. All authors reviewed the manuscript.

Funding Fundação de Amparo à Pesquisa do Estado de São Paulo,2014/50928 - 2,2017/17844 - 8,2019/07007 - 7 and 2019/08582 - 5,2014/50928 - 2,2017/17844 - 8,2019/07007 - 7 and 2019/08582 - 5,2014/50928 - 2,2017/17844 - 8,2019/07007 - 7 and 2019/08582 - 5,2014/50928 - 2,2017/17844 - 8,2019/07007 - 7 and 2019/08582 - 5,2014/50928 - 2,2017/17844 - 8,2019/07007 - 7 and 2019/08582 - 5,Conselho Nacional de Desenvolvimento Científico e Tecnológico,465687/2014 - 8,Fundação Coordenação de Aperfeiçoamento de Pessoal de Nível Superior,Brazil,88887.358273/2019 - 00

Data Availability No datasets were generated or analysed during the current study.

Declarations

Competing Interest The authors declare no competing interests.

References

1. C.T. Kresge, M.E. Leonowicz, W.J. Roth, J.C. Vartuli, J.S. Beck, Nature **359**, 710–712 (1992). https://doi.org/10.1038/359710a0
2. J.S. Beck, J.C. Vartuli, W.J. Roth, M.E. Leonowicz, C.T. Kresge, K.D. Schmitt, C.T.W. Chu, D.H. Olson, E.W. Sheppard, S.B. McCullen, J.B. Higgins, J.L. Schlenker, J. Am. Chem. Soc. **114**, 10834–10843 (1992). https://doi.org/10.1021/ja00053a020
3. D. Zhao, J. Feng, Q. Huo, N. Melosh, G.H. Fredrickson, B.F. Chmelka, G.D. Stucky, Science **279**(5350), 548–552 (1998). https://doi.org/10.1126/science.279.5350.548
4. D. Zhao, Q. Huo, J. Feng, B.F. Chmelka, G.D. Stucky, J. Am. Chem. Soc. **120**, 6024–6036 (1998).
5. Z. Li, L. Liu, Z. Wang, P. Gao, G.K. Li, Energy Fuels **37**, 3413–3427 (2023). https://doi.org/10.1021/acs.energyfuels.2c03882
6. M. Vallet-Regí, F. Schüth, D. Lozano, M. Colilla, M. Manzano, Chem. Soc. Rev. **51**, 5365–5451 (2022). https://doi.org/10.1039/d1cs00659b
7. C.L.P. Oliveira, J.L.S. Lopes, O.A. Sant´Anna, V.F. Botosso, H. N. Bordallo, M.C.A Fantini. J. Phys.Cond. Matter. **34**, 264001 (10pp) (2022). https://doi.org/10.1088/1361-648X/ac6559

8. B. Singh, J. Na, M. Konarova, T. Wakihara, Y. Yamauchi, C. Salomon, M.B. Gawande, Bull. Chem. Soc. Jpn **93**, 1459–1496 (2020). https://doi.org/10.1246/bcsj.20200136
9. J.R. Matos, M. Kruk, L.P. Mercuri, M. Jaroniec, L. Zhao, T. Kamiyama, O. Terasaki, T.J. Pinnavaia, Y. Liu, J. Am. Chem. Soc. **125**, 821–829 (2003). https://doi.org/10.1021/ja0283347
10. C. Yu, Y. Yu, D. Zhao, Chem. Commun. **7**(7), 575–576 (2000). https://doi.org/10.1039/b000603n
11. J.R. Matos, L.P. Mercuri, M. Kruk, M. Jaroniec, Langmuir **18**, 884–890 (2002). https://doi.org/10.1021/la0155294
12. M. Kruk, V. Antochshuk, J.R. Matos, L.P. Mercuri, M. Jaroniec, J. Am. Chem. Soc. **124**, 768–769 (2002). https://doi.org/10.1021/ja0170854
13. C. Yu, Y. Yu, L. Miao, D. Zhao, Micropor. Mesopor. Mater. **44–45**, 65–72 (2001). https://doi.org/10.1016/S1387-1811(01)00169-X
14. J. Fan, C. Yu, F. Gao, J. Lei, B. Tian, L. Wang, Q. Luo, B. Tu, W. Zhou, D. Zhao, Angew. Chem. Int. Ed. **42**, 3146–3150 (2003). https://doi.org/10.1002/anie.200351027
15. L. Huang, X. Yan, M. Kruk, Langmuir **26**(18), 14871–14878 (2010). https://doi.org/10.1021/la102228u
16. J.M. Gómez, M.D. Romero, T.M. Fernández, J. Porous Mater. **17**, 657–662 (2010). https://doi.org/10.1007/s10934-009-9335-y
17. E. Magner, Chem. Soc. Rev. **42**, 6213–6222 (2013). https://doi.org/10.1039/c2cs35450k
18. G. Pota, N. Gallucci, D. Cavasso, I.R. Krauss, G. Vitiello, F. López-Gallego, A. Costantini, L. Paduano, V. Califano, Langmuir **39**, 1482–1494 (2023). https://doi.org/10.1021/acs.langmuir.2c02861
19. B.A. Babalola, A.I. Akinwande, A.A. Otunba, G.E. Adebami, O. Babalola, C. Nwufo, Arab. J. Chem. **17**, 105369 (2024). https://doi.org/10.1016/j.arabjc.2023.105369
20. L. Huang, M. Kruk, Chem. Mater. **27**, 679–689 (2015). https://doi.org/10.1021/cm5028749
21. F.A.N. Nambu, F.G. Corazza, M.D. Duque, P.S. Lopes, V.R. Leite-Silva, N. Andréo Filho, Res. J. Pharmaceut. Biol. Chem. Sci. **10**, 112–122 (2019). https://doi.org/10.33887/rjpbcs/2019.10.6.14
22. A. P. Hammersley, ESRF Internal Report, ESRF97HA02T, ``FIT2D: An Introduction and Overview'', (1997).
23. C.L.P. Oliveira, J. S. Perdersen, unpublished.
24. S. Brunauer, P.H. Emmett, E. Teller, J. Am. Chem. Soc. **60**(2), 309–319 (1938). https://doi.org/10.1021/ja01269a023
25. M. Krug, M. Jaroniec, M. Sayari, Langmuir **13**(23), 6267–6273 (1997). https://doi.org/10.1021/la970776m
26. J.R. Matos, L.P. Mercuri, M. Kruk, M. Jaroniec, Chem. Mater. **13**, 1726–1731 (2001). https://doi.org/10.1021/cm000964p
27. S. Meoto, N. Kent, M.M. Nigra, M.O. Coppens, Microporous Mesoporous Mater. **240**, 61–66 (2017). https://doi.org/10.1016/j.micromeso.2017.04.045
28. R. Shun-ichi Matsuura, T. Ishii, T. Itoh, S. Hanaoka, T. Hamakawa, F.M. Tsunoda, Microporous Mesoporous Mater. **127**, 61–66 (2010). https://doi.org/10.1016/j.micromeso.2009.06.029
29. D.W. Losito, P.S. Lopes, A.R. Ueoka, M.C.A. Fantini, P.L. Oseliero Filho, N. Andréo-Filho, T.S. Martins, Microporous Mesoporous Mater. **325**, 111316 (2021). https://doi.org/10.1016/j.micromeso.2021.111316
30. T. Jesionowski, J. Zdarta, B. Krajewska, Adsorption **20**, 801–821 (2014). https://doi.org/10.1007/s10450-014-9623-y